Journal of Alloys and Compounds 925 (2022) 166667

Contents lists available at ScienceDirect

Journal of Alloys and Compounds

journal homepage: www.elsevier.com/locate/jalcom

Research article

A novel synergy of Co/La co-doped porous $BiVO_4$ photoanodes with enhanced photoelectrochemical solar water splitting performance

Huimin Geng[a], Sheng Huang[a], Dan Kong[a,b], Eugene Chubenko[c], Vitaly Bondarenko[c], Pengzhan Ying[a], Yanwei Sui[a], Yulong Zhao[a,*], Xiuquan Gu[a,b,**]

[a] School of Materials and Physics, China University of Mining and Technology, Xuzhou 221116, People's Republic of China
[b] Jiangsu Province Engineering Laboratory of Highly Efficient Energy Storage Technology and Equipment, Xuzhou 221116, People's Republic of China
[c] Belarusian State University of Informatics and Radioelectronics, 220013P, Brovka str. 6, Minsk, Belarus

ARTICLE INFO

Article history:
Received 17 May 2022
Received in revised form 1 August 2022
Accepted 4 August 2022
Available online 5 August 2022

Keywords:
$BiVO_4$ photoanode
Co-doping
La-doping
Photoelectrochemical
Water splitting

ABSTRACT

This work discussed a straightforward approach to manufacture Co-, La-, and Co/La-doped $BiVO_4$ nanoporous films. The effect of doping in the photoelectrochemical (PEC) water splitting performance was evaluated through PEC test and the strong electronic correlation of the framework in the density functional theory (DFT) calculation was taken into account. It was shown that replacing Bi atoms with Co would decrease the bandgap of $BiVO_4$, but doping with La shifted the bandgap from indirect to direct and resulted in the negative shift of onset potential. Furthermore, doping Co and La ions into $BiVO_4$ also introduced deep levels into the $BiVO_4$ bandgap. After the optimization of the mole ration of Co to La, the (0.7/0.3)Co/La:$BiVO_4$ photoanode achieved a high photocurrent density of 3.65 mA cm^{-2} under the simulated solar irradiation with a bias of 1.23 V_{RHE}, resulting in an H_2/O_2 production rate of 57.6/25.8 μmol cm^{-2} h^{-1}. More importantly, without any co-catalysts and hole scavengers, the photoanode presented a favorable stability during 16 h test. The enhanced PEC performance was mainly due to improved visible light absorption and carrier separation ability. Both the experimental and theoretical demonstrations proved that the dual-element doping strategy shed light on designing efficient and stable photoelectrodes for solar energy conversion.

1. Introduction

Photoelectrochemical (PEC) technology has attracted extensive attention due to its potential applications in energy conservation and environmental protection, which can transform solar energy into clean hydrogen energy through splitting water [1–5]. In PEC water splitting process, the photoanode is excited by light to generate and separate electron-hole pairs, and then oxygen evolution reaction (OER) and hydrogen evolution reaction (HER) occurs at both surfaces of the photoanode and counter electrode, respectively [6–9]. Among various semiconductors, bismuth vanadate ($BiVO_4$) has been considered as one of the most promising photoanodic materials for solar-driven water splitting due to its suitable bandgap of ~ 2.4 eV, allowing the solar energy to be utilized efficiently, and relatively positive valence band edge, providing a sufficient overpotential for water photo-oxidation [10–14].

Under Air Mass 1.5 Global (AM 1.5 G) standard test conditions, the theoretical limit on solar-to-hydrogen (STH) conversion efficiency of a $BiVO_4$ photoanode is 9.1% at a maximum photocurrent density of 7.5 mA cm^{-1}-2 [15,16]. However, the actual PEC performance of $BiVO_4$ is much lower than the theoretical value due to severe photocarrier recombination losses and sluggish water oxidation kinetics [17–20]. Additionally, $BiVO_4$ is also highly photocorrosive and the dissolution of V^{5+} ions from $BiVO_4$ lattice into electrolyte is responsible for its behavior [21,22]. Up to now, various strategies have been tried to improve the PEC activity and stability of the $BiVO_4$ photoanode, including morphology control, surface modification, element doping, and so on [23,24]. In 2014, Kim and Choi reported the preparation of a nanoporous $BiVO_4$ anode through a method comprising the electrodeposition of a bismuth oxyiodide (BiOI) film and its subsequent impregnation with a dimethyl sulfoxide (DMSO) solution containing vanadium source [25]. The obtained $BiVO_4$ electrode possessed a worm-like morphology, resulting in large specific surface area and high carrier mobility. Wang et al. have shown that the deposition of the Fe/Co oxide catalyst into a

* Corresponding author.
** Correspondence to: School of Materials Science and Physics, China University of Mining and Technology, China.
E-mail addresses: sdyulong@cumt.edu.cn (Y. Zhao), xqgu@cumt.edu.cn (X. Gu).

https://doi.org/10.1016/j.jallcom.2022.166667
0925-8388/

$BiVO_4$ porous film exhibited a photocurrent density of 4.82 mA cm^{-2} at 1.23 V_{RHE} under the AM 1.5 G solar illumination, and no obvious decay was observed in the 10 h test [26]. Further on, He et al. demonstrated a high photocurrent density of 6.34 mA cm^{-2} at 1.23 V_{RHE} in specifically developed NiOOH/FeOOH/Co_3O_4/$BiVO_4$ photoanodes under the near-infrared (NIR) irradiation, corresponding to ~ 85% of the theoretical value for the pure $BiVO_4$ photoanode [27]. As far as we know, this might be the highest PEC efficiency based on $BiVO_4$ photoanode reported to date. Recently, our research group modified the $BiVO_4$ photoanode with FeOOH and Au nanoparticles, leading to a photocurrent density of 4.64 mA cm^{-2} at 1.23 V_{RHE} under the simulated solar irradiation [28].

Nevertheless, without further co-catalyst modification or employing a hole scavenger, the photocurrent densities of the $BiVO_4$-based photoanodes are still unsatisfactory. In view of this, elemental doping is another way to enhance the PEC performance of a semiconductor electrode. Mo and W are the most commonly used substituent elements for vanadium in the $BiVO_4$ lattice, which will lower the small polaron hopping barrier, thus improving major carrier density and promoting charge mobility [29–33]. Furthermore, the defect states created in the bandgap of $BiVO_4$ by W or Mo dopants can also contribute to increase the active sites at the $BiVO_4$ surface for the water oxidation. Yang et al. demonstrated that the Mo doped $BiVO_4$ photoanode produced a photocurrent density of 1.91 mA cm^{-2} at 1.23 V_{RHE} for the water oxidation that was almost 2.33 times higher than that of pure $BiVO_4$ [29]. In Liu's study, W doping could generate oxygen vacancies (O_V) as electron donors in bulk $BiVO_4$, leading to a photocurrent density of ~ 4.4 mA cm^{-2} at 1.23 V_{RHE} and long-term stability for 25 h without any co-catalysts [31]. Moreover, researchers have also finished a lot of work on the effect of dual-element doping (co-doping) in the PEC activity and stability of the $BiVO_4$ photoanodes. For example, Tayebi et al. reported the fabrication of W/Mo codoped $BiVO_4$ photoanodes, which displayed the improved PEC performance after optimizing the W/Mo ratio [32]. Prasad et al. reported a novel two-dimensional (2D) heterojunction photoelectrode composed of WO_3 and (Er,W):$BiVO_4$ for solar-driven water oxidation, where Er and W atoms substituted Bi and V atoms in $BiVO_4$, respectively [33]. As a result, the high photocurrent density of 4.1 mA cm^{-2} and charge separation efficiency of 93% were achieved at 1.23 V_{RHE}. However, so far there have been no reports of Bi being co-substituted with Co- and La- ions in the $BiVO_4$ lattice to enhance the PEC activity of $BiVO_4$ photoanodes.

Herein, the following work focused on adopting a facile route for developing the Co/La co-doped $BiVO_4$ (Co/La: $BiVO_4$) nanoporous films for the PEC water splitting. The electronic structures of the doped samples were simulated by density functional theory (DFT). Both Co and La elements were incorporated into the $BiVO_4$ lattice simultaneously. The Co/La: $BiVO_4$ photoanode demonstrated the photocurrent density of 3.65 mA cm^{-2} at 1.23 V_{RHE} under simulated solar irradiation, being nearly 3 times higher than that of undoped $BiVO_4$ anodes (1.25 mA cm^{-2}). Impressively, such a photocurrent value was achieved under a condition without any co-catalysts and hole scavengers (such as methanol, sodium sulfite), while the photoanode presented a favorable stability during 16 h test. The excellent PEC performance could be attributed to the enhancements of visible light absorption and charge separation. After the Co/La co-doping, the bandgap of $BiVO_4$ was decreased slightly and switched from indirect to direct, while the onset potential was lowered. The low onset potential was attractive for constructing a non-biased PEC water splitting system.

2. Experimental section

2.1. Preparation of $BiVO_4$ electrodes

The nanoporous $BiVO_4$ electrodes were prepared following the reported procedure [25]. First, a 0.04 mol/L $Bi(NO_3)_3$ solution was prepared by slowly dissolving $Bi(NO_3)_3$•5 H_2O in 50 mL of the 0.4 mol/L KI aqueous solution with pH value of 1.75. Then, 20 mL of absolute ethanol containing 0.23 mol/L p-benzoquinone was mixed into the solution. The BiOI electrodeposition onto a FTO glass substrate was carried out in a three-electrode electrochemical cell consisting of a working (WE), counter (CE) and reference (RE) electrodes at − 0.143 V *vs*. saturated calomel electrode (SCE) for 10 min. Then, 0.15 mL of $VO(acac)_2$/DMSO solution (0.2 mol/L) was dripped onto the BiOI films (2 × 2 cm^2), which were followed by drying in an oven (60 °C, 3 h) and annealing in air (450 °C, 2 h). Finally, the pristine $BiVO_4$ electrodes were obtained by soaking the samples into a 1.0 mol/L NaOH aqueous solution for 30 min to remove the excess of V_2O_5.

2.2. Preparation of Co, La mono- and La/Co co-doped $BiVO_4$ electrodes

The fabrication of La/Co co-doped $BiVO_4$ photoanodes follows a similar method to that of the pure nanoporous $BiVO_4$ one. As a typical demonstration, the fabrication process of nanoporous La/Co co-doped $BiVO_4$ photoanodes is depicted in Scheme 1. Typically, for preparing the 1.0Co:$BiVO_4$ electrode, the BiOI electrode was immersed in DMSO solution containing 0.2 mol/L $VO(acac)_2$ and 1.0 mmol/L $Co(acac)_2$, followed by the calcination process. Similarly, a 1.0La:$BiVO_4$ electrode was obtained by dipping a DMSO solution containing $VO(acac)_2$ and $La(acac)_3$ onto the BiOI film. To form Co/La:$BiVO_4$ samples, the DMSO solutions with various concentrations of dissolved $Co(acac)_2$, $La(acac)_3$ and $VO(acac)_2$ were used. For instance, during the formation of the 0.7Co/0.3La:$BiVO_4$ sample, the molar concentrations of $Co(acac)_2$, $La(acac)_3$ and $VO(acac)_2$ were set to 0.7 mmol/L, 0.3 mmol/L and 0.2 mol/L, respectively. Thus, the 0.5Co/0.5La:$BiVO_4$ and 0.3Co/0.7La:$BiVO_4$ were obtained by following the same procedure.

2.3. Material characterization

The structural analysis of samples was implemented by X-ray diffractioner (XRD, Haoyuan DX-2700) with a Cu Kα source. The surface morphology and microstructure were determined by a high-resolution transmission electron microscopy (HRTEM, Tecnai G2F20) and a field-emission scanning electron microscopy (FESEM, Hitachi New Generation SU8220, Japan) equipped with an X-ray energy

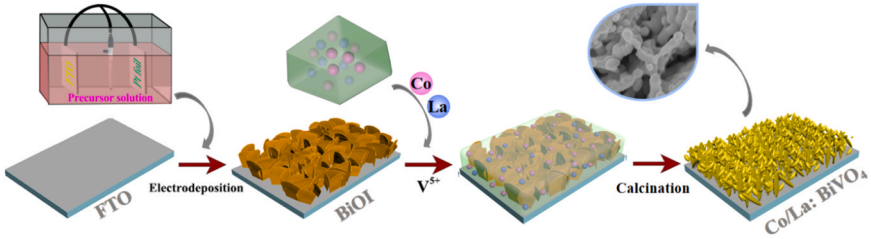

Scheme 1. Technological steps for the fabrication of nanoporous La/Co:$BiVO_4$ electrodes.

dispersive spectrometer (EDS). The optical absorption spectra of the samples were obtained with an UV–vis diffusion reflectance spectrophotometer (DRS, Cary 300, Varian Co.), in which $BaSO_4$ was used as the internal reflectance standard. Both the surface element compositions and chemical valence states were analyzed by a X-ray photoelectron spectroscopy (XPS, EscaLab 250Xi) with an Al Kα source. The time-resolved photoluminescence (TRPL) spectra were recorded using an Edinburgh FS5 spectrophotometer.

2.4. PEC measurements

The PEC performance was measured using a CHI 660E electrochemical workstation with a 500 W Xe lamp (CHF-XM-500 W, Beijing Changtuo Technology Co., Ltd.) as the irradiation source. The photoanode, a SCE and a Pt foil were used as WE, RE and CE, respectively. The intensity of the simulated sunlight was adjusted to 1 sun (100 mW/cm^2) with a standard reference silicon solar cell. The potential-dependent transient photocurrent plots were obtained by linear sweep voltammetry (LSV) at a sweeping rate of 20 mV/s. Incident photoelectron conversion efficiency (IPCE) was obtained in 0.1 mol/L Na_2SO_4 under a constant potential of 1.23 V_{RHE} with a LED power supply and calculated using the equation (see Eq. (1) in Supplemental Information (SI)). Electrochemical impedance spectra (EIS) were recorded under irradiation over a frequency range of 0.1–5 × 10^4 Hz with an amplitude of 20 mV and an applied potential of 0.0 V *vs*. SCE. The applied bias photon-to-current efficiency (ABPE) could be calculated using the equation (see Eq. (2) in SI). The measured potential *vs*. SCE was converted to that *vs*. Reversible Hydrogen Electrode (RHE) according to the Nernst equation (see Eq. (3) in SI).

2.5. DFT calculation details

The structure relaxation and electronic structure for all the samples were calculated by the PWmat software [34,35]. The structure relaxation was performed using the generalized gradient approximation of Perdew-Burke-Ernzerhof (PBE) [36]. During structure optimization, all structures were relaxed until the force acting on each atom was less than 0.01 eV/Å. A 8 × 8 × 8 Gamma-centered k-points grid was chosen in the calculations. The NCPP-SG15-PBE pseudopotentials was assumed for all calculations with an energy cutoff of 50 Ryd [37].

3. Results and discussion

Both Fig. 1(a) and S1(a) display the SEM images of the pristine $BiVO_4$ nanoporous film, which consist of many bound nanoparticles with an average length of about 500 nm and a width of 100–200 nm. Obviously, the nanoporous structure facilitates the electrolyte infiltration and photogenerated carrier transport. After La and Co co-doping, the surface of the $BiVO_4$ nanoporous films become

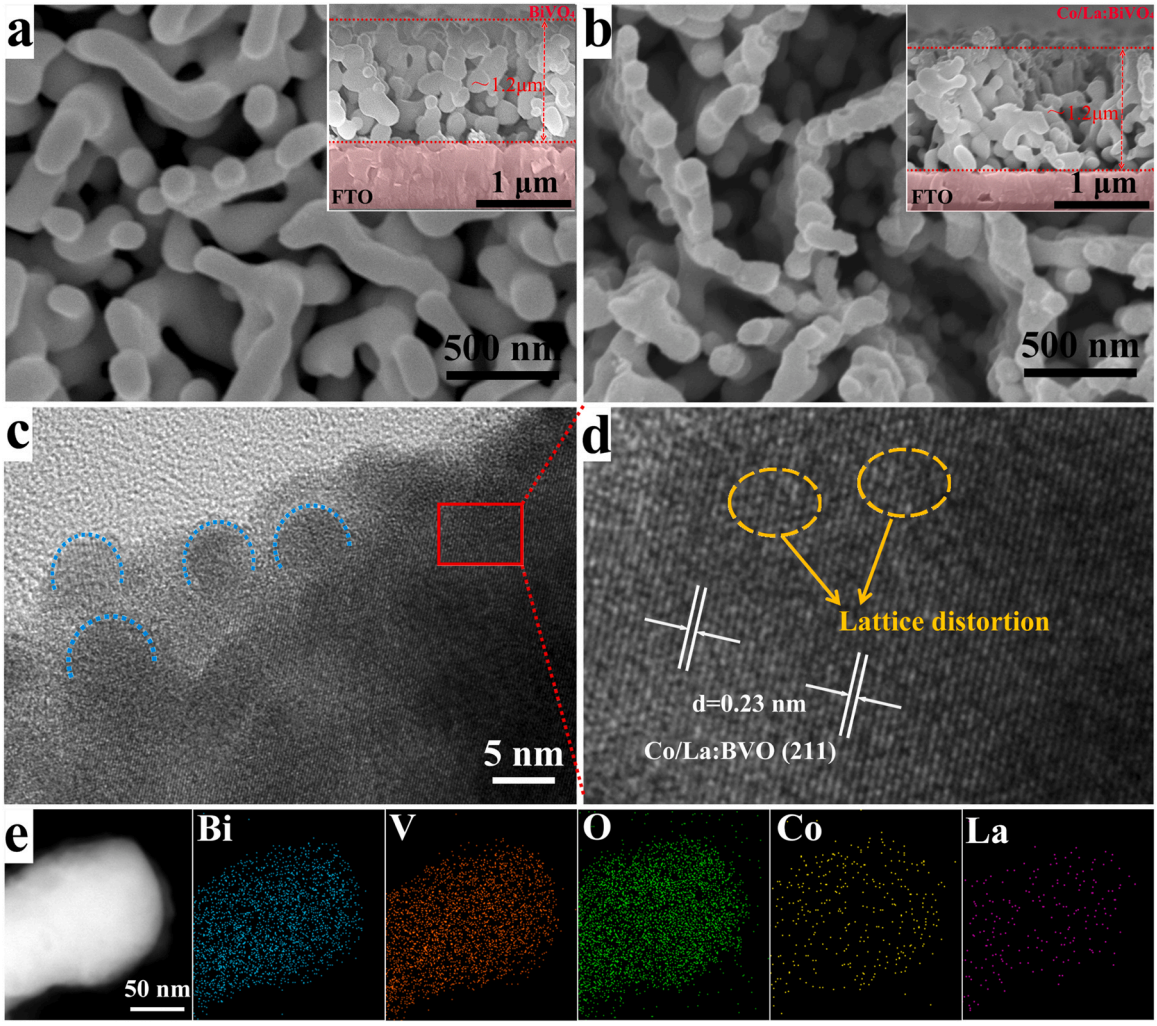

Fig. 1. FESEM images of (a) pristine $BiVO_4$ and (b) Co/La:$BiVO_4$ films. The insets in (a) and (b) show the cross-sectional SEM images of the corresponding samples. (c) TEM, (d) HRTEM and (e) EDS mapping images of Co/La:$BiVO_4$ with a Co/La molar ratio of 7: 3.

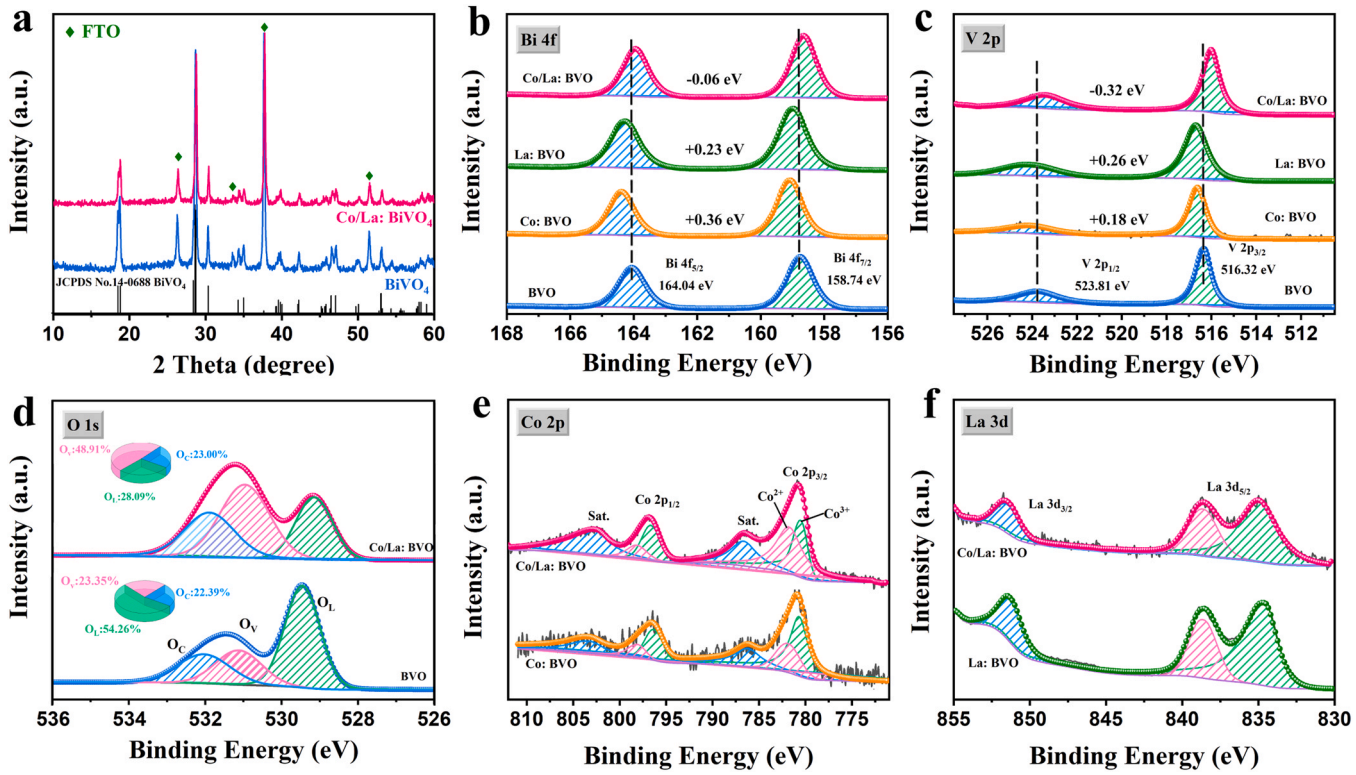

Fig. 2. (a) XRD patterns of $BiVO_4$ and Co/La:$BiVO_4$ samples. XPS spectra of $BiVO_4$, Co:$BiVO_4$, La:$BiVO_4$ and Co/La:$BiVO_4$ samples: (b) Bi 4 f, (c) V 2p, (d) O 1 s, (e) Co 2p, and (f) La 3d, the inset in (d) shows the atomic ratios of O_L, O_V and O_C.

considerably rougher with smaller grain sizes (Fig. 1(b) and S1(b)). Meanwhile, according to the insets of Figs. 1a and 1(b), the two samples display almost the same film thickness of ~ 1.2 μm.

In order to reveal the mechanism for morphology changes, the top-view FESEM images of Co:$BiVO_4$ and La:$BiVO_4$ samples are compared (Fig. S2). It is observed that the Co doping has a significant influence on the $BiVO_4$ morphology, whereas the La doping fails to show significant effect. This behavior can be explained by the closer ionic radius of La^{3+} (0.106 nm) and Bi^{3+} (0.108 nm) than that of Co^{2+}/Co^{3+} (0.074/0.063 nm). Fig. 1(c) also shows the TEM image of Co/La:$BiVO_4$ nanoparticles that are scraped from the FTO substrate. The nanoporous film has a rough surface and is actually composed of a lot of fine grains with an average size of ~ 5 nm. As displayed in the partially enlarged image (Fig. 1(d)), the lattice fringes show an interplanar spacing of ~0.23 nm, corresponding to the (211) planes of monoclinic $BiVO_4$. This result once again confirms that the doping does not destroy the crystal structure of $BiVO_4$. Certainly, a small lattice distortion is observed from the doping (Fig. S3). That is to say, the doping reduces the lattice order of monoclinic $BiVO_4$ crystal. Fig. 1(e) shows the EDS mapping images of Co/La:$BiVO_4$, in which the Co and La elements are distributed uniformly in the whole grain. In terms of the EDS pattern (Fig. S4), the Co and La elements exhibit the atomic contents of 1.40% and 0.61% in the 0.7Co/ 0.3La:$BiVO_4$ samples, which is consistent with the nominal Co/La ratio (0.7 mmol/L *vs.* 0.3 mmol/L) in the precursor solution. It is well known that EDS is only a surface analysis method, so it is difficult to obtain the element content in the sample. Therefore, the ICP-MS measurement was applied, and a molar Co/La ratio of 1:0.47 (≈ 7:3) is achieved in the co-doped samples. That means the percentages of Co and La in the composite photoanode were 0.65% and 0.30%, respectively. Obviously, the element contents obtained by the ICP-MS measurement is consistent with the EDS results.

Fig. 2(a) and Fig. S5 show the XRD patterns of four samples including $BiVO_4$, Co:$BiVO_4$, La:$BiVO_4$ and Co/La:$BiVO_4$. When doped with Co and La, no significant changes are observed in the XRD patterns compared to the pristine $BiVO_4$ film. Simultaneously, no peaks corresponding to the CoO_x and LaO_x are detected. The analysis result indicates that the monoclinic $BiVO_4$ phase persists after incorporating Co and La into the lattice due to the low doping amounts of La and Co (0 ~ 2 at%) source precursors.

Afterwards, in order to further investigate the doping situation of metal ions, high-resolution XPS spectra are performed on these samples (Fig. 2(b-f)). Both the Co and La elements are identified in the XPS spectra of the co-doped $BiVO_4$ sample, indicating that these two elements have been successfully incorporated into the material. For the pristine $BiVO_4$ sample, two characteristic peaks located at 164.04 and 158.74 eV are observed arising from Bi 4 $f_{5/2}$ and Bi 4 $f_{7/2}$ signals, indicating that the Bi ions are in the oxidation state Bi^{3+}. The two asymmetric peaks located at 523.81 and 516.32 eV are observed arising from V $2p_{1/2}$ and V $2p_{3/2}$ signals, indicating that the V ions are in the oxidation state V^{5+}. Compared to the pristine $BiVO_4$, the Bi 4 f and V 2p core-level peaks of both Co:$BiVO_4$ and La:$BiVO_4$ shift to higher binding energies, which may be due to the interactions of dopant atoms (*e.g.*, Co and La) with Bi and V atoms. This provides a piece of direct evidence that La and Co have been embedded into the $BiVO_4$ lattice. Nevertheless, it is surprising that both the Bi 4 f and V 2p core-level peaks of $BiVO_4$ shift to lower binding energies after co-doping with Co and La. The XPS peak shifts of mono-doped and co-doped samples show different characteristics. It is generally believed that the lower the chemical binding energy, the weaker the ability of elements to share electrons, implying that there might be more electrons inside the Co/La:$BiVO_4$ sample participated in the photocatalytic reaction than mono-doped ones. As shown in Fig. 2(d) and Fig. S6, the O 1 s spectra are fitted into three peaks of 529.5, 531.2 and 532.1 eV, which are assigned to the lattice oxygen (O_L), the oxygen vacancy (O_V) and the chemisorbed or dissociated oxygen species (O_C), respectively. The O_V peaks of doped $BiVO_4$ have a higher intensity than the pristine $BiVO_4$. The relative O_V percentage (to O

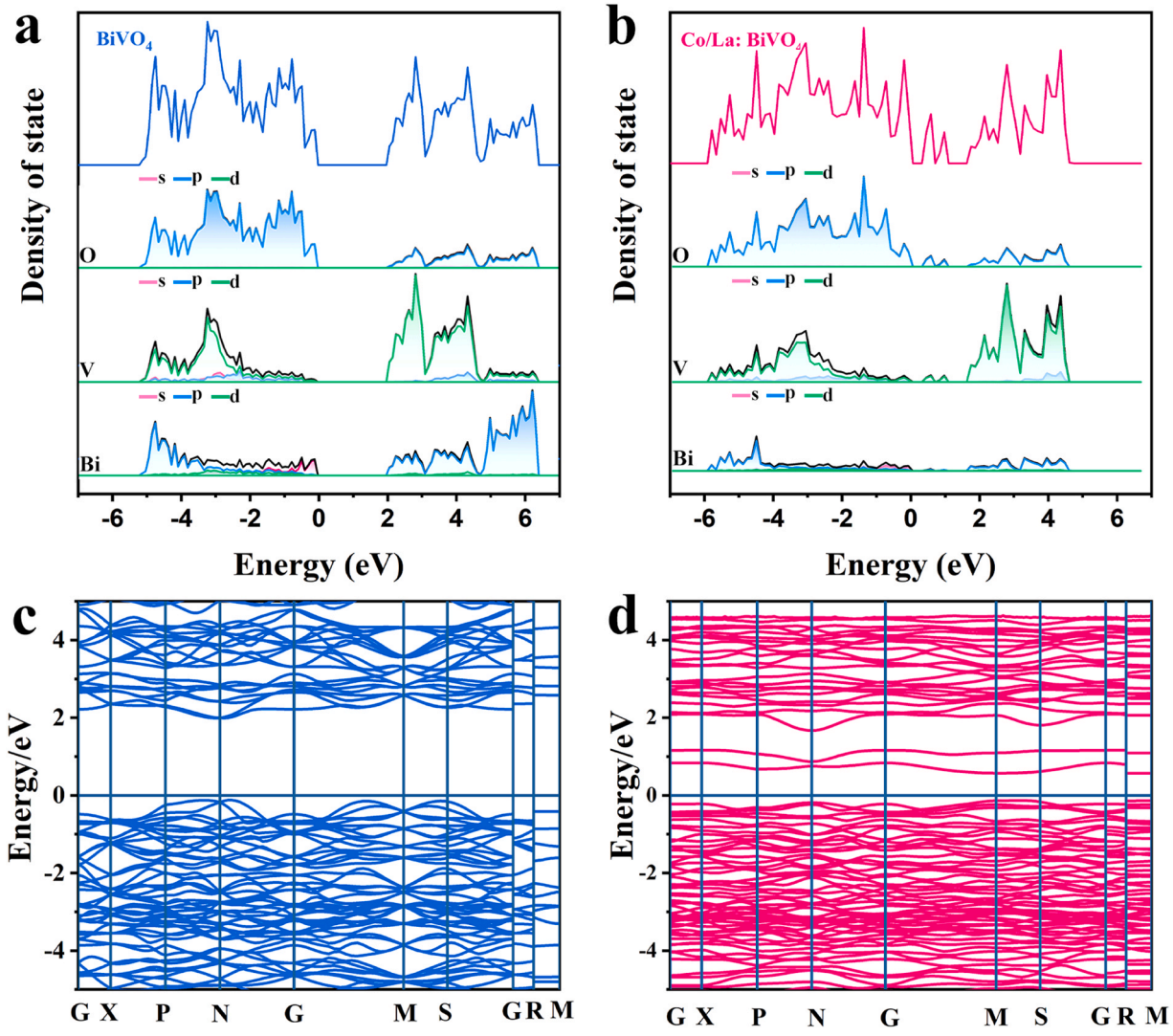

Fig. 3. DFT calculation results: DOS of pristine (a) $BiVO_4$ and Co/La:$BiVO_4$ (b) samples; band structure characteristics of (c) $BiVO_4$ and (d) Co/La:$BiVO_4$ samples.

atoms) increases from 23.35% to 48.91% after a co-doping of Co and La. Apparently, these O_V defects are caused by Co and La doping, which is quite similar to previously reported data on W:$BiVO_4$ [31]. When fitting the Co 2p spectra (Fig. 2(e)), the two characteristic peaks at 781.85 and 780.60 eV are attributed to the oxidation states Co^{2+} and Co^{3+} in Co $2p_{3/2}$, indicating that the samples contain Co^{2+}/Co^{3+} species. The binding energies of La $3d_{3/2}$ and La $3d_{5/2}$ peaks at 851.4 and 838.5 eV confirm the successful doping of La in $BiVO_4$ and the existence of the La ions in a form of La^{3+} (Fig. 2(f)).

To further understand the advantages of the Co/La co-doping, the DFT calculations are discussed. The theoretical calculation models shown in Fig. S7 exhibit the doping positions of the Co and La elements in the lattice. The density of states (DOS) is firstly calculated to explore the change in the electronic structures as illustrated in Fig. 3(a, b). For the stoichiometric $BiVO_4$, the calculated bandgap is around 2.03 eV (Fig. 3(a)) that is close to the theoretical value (2.4 eV). When the Co and La atoms are introduced into the $BiVO_4$ in suitable ratios, the shape of total DOS does not vary evidently, except that several defect levels appear in the bandgap. The DOS result also suggests that the conduction band and valence band of $BiVO_4$ are dominated by the V and O elements, respectively. As it can be seen from the electronic structure (Fig. 3(c, d)), $BiVO_4$ exhibits an indirect bandgap characteristic, while the Co/La:$BiVO_4$ shows a direct bandgap. Apparently, the direct bandgap semiconductor has a higher absorption coefficient than the indirect one. Besides, the bandgap of $BiVO_4$ tends to decrease after co-doping with Co/La, while two deep levels are clearly observed in the Co/La:$BiVO_4$ sample. The deep levels facilitate the electron transition and the enhancement of visible light absorption [38]. In order to further explore the causes of these phenomena, DFT calculation results of Co:$BiVO_4$ and La:$BiVO_4$ are compared (Fig. S9). It is illustrated that Co doping is the main factor affecting the decrease of $BiVO_4$ bandgap, whereas La doping changes the type of bandgap (from indirect to direct). Meanwhile, it is also proved that the deep levels are induced by the Co/La co-doping, because the two deep levels are not observed in the Co:$BiVO_4$ and La:$BiVO_4$ samples.

In order to further study the effect of Co and La doping on the light absorption of $BiVO_4$, the UV–vis absorption spectra of all samples are displayed in Fig. S10(a). All samples demonstrate a sharp absorption edge around 470 nm, which corresponds to the bandgap (~ 2.4 eV) of $BiVO_4$. After 500 nm, the Co doping significantly enhances the visible light absorption in $BiVO_4$, whereas the La doping has almost no effect on the light absorption. The obtained 0.7Co/0.3La:$BiVO_4$ sample has stronger visible light absorption than pristine $BiVO_4$. Subsequently, Fig. S11 also compares the absorption spectra of 0.7Co/0.3La:$BiVO_4$ with 0.7Co:$BiVO_4$. It can be seen that the 0.7Co/0.3La: $BiVO_4$ sample displays slightly higher visible light absorption than the 0.7Co: $BiVO_4$ one, which may be due to the deep

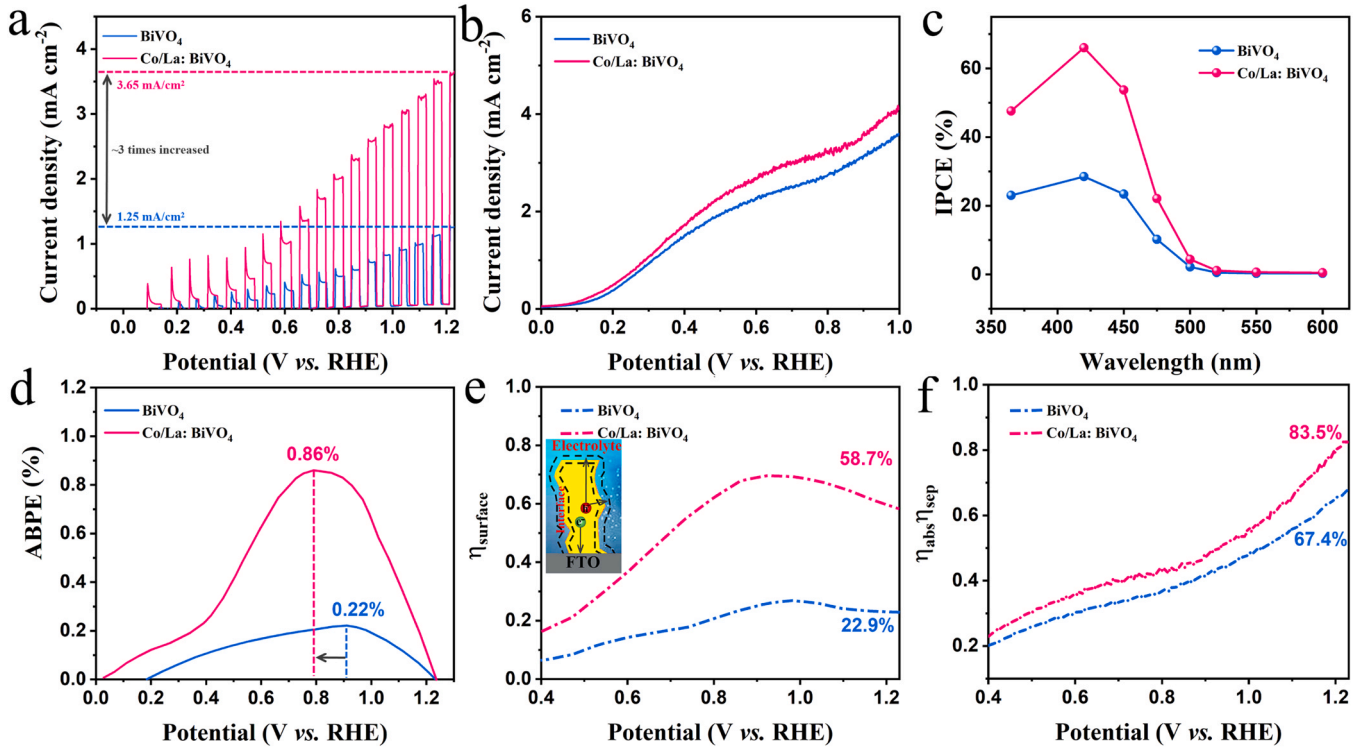

Fig. 4. (a) LSV plots measured in 0.1 M Na_2SO_4 under a chopped irradiation, (b) LSV plots measured in 0.1 M Na_2SO_4/Na_2SO_3 under continuous irradiation, (c) IPCE spectra, (d) ABPE plots, (e) surface separation efficiency, and (f) bulk charge separation efficiency of $BiVO_4$ and Co/La:$BiVO_4$ samples.

level caused by co-doping of Co and La. The result is consistent with the above DFT calculation results. Besides, we also investigate the effect of doping with a series of elements such as Fe, La, Mo, Co and Sc on the PEC performance of $BiVO_4$, as illustrated in Fig. S12. It can be clearly seen from the plots that doping with Co can maximize the PEC performance of the $BiVO_4$ film. The effect of La doping is only second to Co doping, but better than other elements such as Fe, Mo, Sc, and so on. Moreover, La doping can significantly lower the initial potential of $BiVO_4$ photoanodes. Thus, based on a comprehensive consideration, we choose codoping of La and Co to improve the PEC performance of $BiVO_4$.

Fig. 4 shows the PEC performance of Co/La:$BiVO_4$ photoanodes under AM 1.5 G. The optimum Co/La ratio is found to be 7/3 for the Co/La:$BiVO_4$ samples (Fig. S13). Namely, the feed ratio of the Co salt to the La salt is 7/3 in the process of precursor solution. Specifically, the photoanode (0.7Co/0.3La:$BiVO_4$) achieves a relatively higher photocurrent density of ~ 3.65 mA cm^{-2} at 1.23 V_{RHE} compared with others. When the cocatalyst is modified, the Co/La:$BiVO_4$-FeOOH photoanode exhibited the highest photocurrent density of 4.9 mA cm^{-2} at 1.23 V_{RHE} (Fig. S14) among all the samples. In contrast, the photocurrent of pristine $BiVO_4$ is just 1.25 mA cm^{-2} at 1.23 V_{RHE}. These results indicate that the photoanodes have better water oxidizing ability upon modification of FeOOH, which is a common cocatalyst for enhancing the PEC performance, as reported in the previous work [28]. As summarized in Table S1, the increased PEC activity of this work is comparable or even higher than those reported in other reports, suggesting the Co/La co-doping is an efficient route for improving the PEC performance. Furthermore, it can be seen from the enlarged view of some areas in Fig. S13 that the onset potential of $BiVO_4$ become more negative as the ratio of La increases. The optimum photoanode exhibits a lower onset potential (0.1 V_{RHE}) than pristine $BiVO_4$ (0.2 V_{RHE}). As far as we know, the low turn-on voltage is very useful for creating a two-electrode, unbiased solar water splitting device [39,40]. Fig. 4(b) shows the LSV plots of $BiVO_4$ and Co/La:$BiVO_4$ photoanodes measured in a 0.1 mol/L Na_2SO_4 with 0.1 mol/L Na_2SO_3 solution as a hole scavenger under the solar irradiation. Apparently, the photocurrent densities of both samples are significantly enhanced due to the higher charge separation efficiency. Nevertheless, it is worth noting that the effect of Na_2SO_3 adding on the photocurrent of the Co/La:$BiVO_4$ is significantly weaker than that of the pristine $BiVO_4$, suggesting that the former possesses stronger carrier separation ability than the later even without any scavengers and co-catalysts. The strong carrier separation ability of the Co/La:$BiVO_4$ might be related to the oxygen defects induced by doping.

Fig. 4(c) shows a comparison of the IPCE spectra of the pristine $BiVO_4$ and Co/La:$BiVO_4$ samples. The IPCE spectra of two samples are consistent with their UV–vis absorption spectra. The IPCE value of the Co/La:$BiVO_4$ reaches up to 66% at 420 nm, vastly higher than that of pristine $BiVO_4$ (28.5%). In addition, the ABPE values of the pristine $BiVO_4$ and Co/La:$BiVO_4$ photoanodes are calculated (see Eq. (2) in SI) as presented in Fig. 4(d). The Co/La:$BiVO_4$ displayed the maximum ABPE value of 0.86% at a low potential of 0.8 V_{RHE}, which was nearly 4 times higher than pristine $BiVO_4$ (only 0.22% at 0.91 V_{RHE}). To provide direct evidence that the co-doping contributes to the acceleration of the charge separation, we also calculate the surface separation efficiency ($\eta_{surface}$) and the bulk charge separation efficiency ($\eta_{abs}\eta_{sep}$) by combining the data of Fig. 4(a, b) (see Eq. (4, 5) in SI). The detailed calculation results are shown in Fig. 4(e, f). As can be seen, the $\eta_{surface}$ and $\eta_{abs}\eta_{sep}$ of Co/La:$BiVO_4$ are significantly higher than those of pristine $BiVO_4$, what may be due to the contribution of the oxygen defects induced by doping. But the change in surface separation efficiency is more obvious than that of bulk charge separation efficiency on Co/La:$BiVO_4$, which means that the interface structure between electrode/electrolyte is the main essential factor that improves its PEC performance for water oxidation. To investigate the surface carrier charge transfer process of the photoelectrodes, the open circuit photovoltage (OCP = OCP_{light} - OCP_{dark}) test is performed. Essentially, the photovoltage is the difference between the quasi-electronic Fermi level ($E_{F,n}$) and the quasi-hole

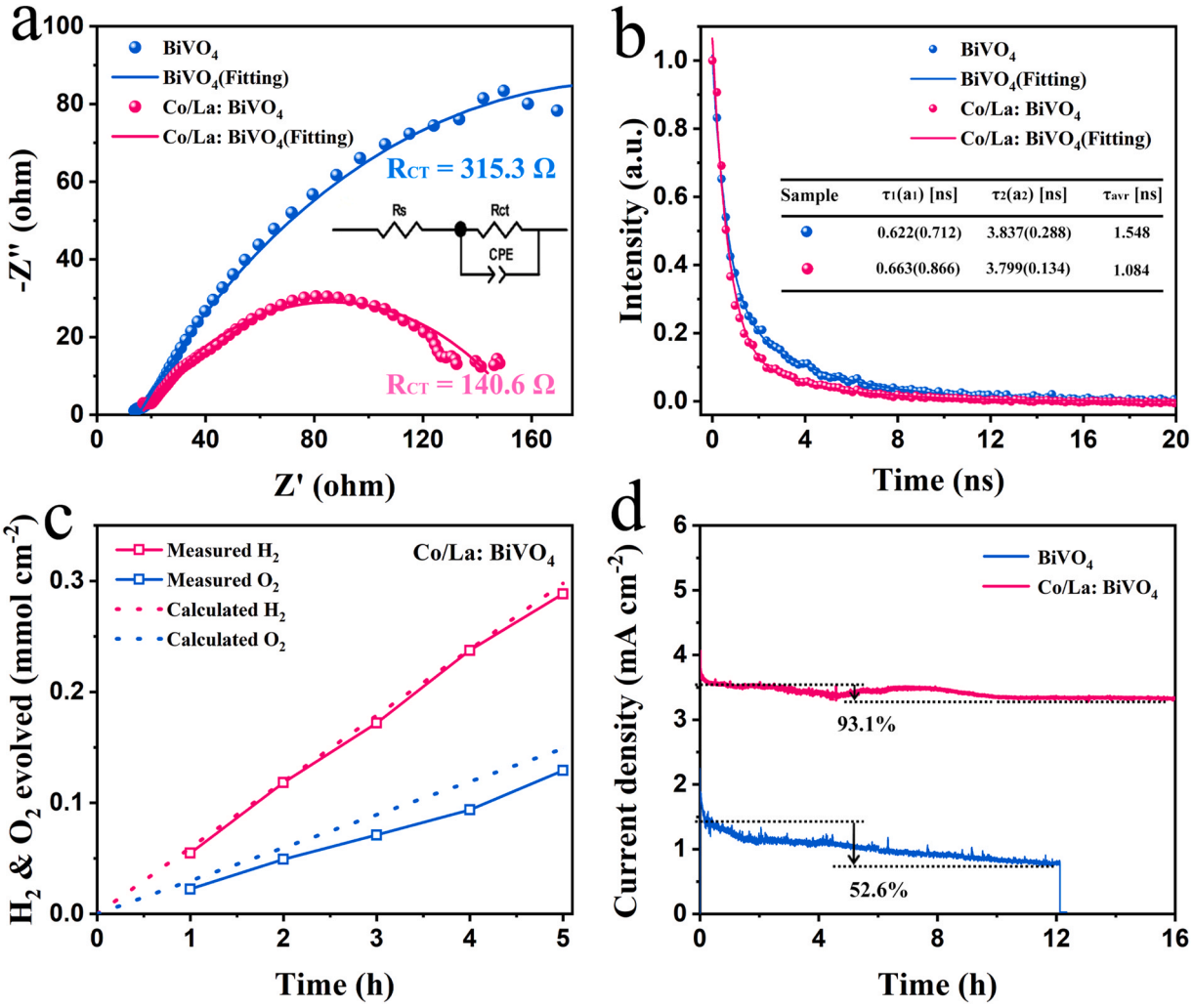

Fig. 5. (a) Nyquist plots of the EIS spectra, (b) transient TRPL spectra, (c) time course of PEC hydrogen and oxygen evolution and (d) long-term J-t plots for the $BiVO_4$-based photoanodes. The inset in (a) is an equivalent circuit model for fitting Nyquist plots.

Fermi level ($E_{F,p}$), however, the presence of surface states causes the Fermi level pinning effect to bring about a decrease in photovoltage [41]. Clearly, as shown in Fig. S15, the Co/La:$BiVO_4$ photoanode has the larger OCP compared with the pristine $BiVO_4$ electrode, indicating that doping has an influence on surface states elimination, which diminishes Fermi level pinning behavior, therefore would incur larger band bending and fast charge transfer at the electrode-electrolyte interface.

The EIS spectra are recorded to gain more insight into the mechanism underlying the high performance of Co/La:$BiVO_4$ photoanodes. Fig. 5(a) displays a comparison the Nyquist plots of pristine $BiVO_4$ and Co/La:$BiVO_4$ photoanodes. Among them, the arch shows the kinetics of charge transfer in the photoelectrode, whereas the semicircle diameter represents the charge transfer resistance (R_{CT}) from the impedance at the solid/liquid interfaces. Apparently, the Co/La:$BiVO_4$ photoanode owns the smaller semicircle diameter, implying that the co-doped sample demonstrates a much lower R_{CT} value than the pristine $BiVO_4$ one. The fitted results show that the R_{CT} values of pristine $BiVO_4$ and Co/La:$BiVO_4$ are 315.3 and 140.6 Ω, respectively. This may be due to the oxygen defects induced by the Co/La co-doping, which acts as photocatalytic active sites and leads to a reduction of the charge transfer resistance. Furthermore, the M-S plots of different samples are obtained in dark (Fig. S16). By terms of the M-S analysis, the charge carrier density (N_D), in which the N_D values are 14.9×10^{18} cm^{-3}, 16.3×10^{18} cm^{-3}, 20.3×10^{18} cm^{-3}, and 27.3×10^{18} cm^{-3} for $BiVO_4$, La:$BiVO_4$, Co:$BiVO_4$, and Co/La:$BiVO_4$ electrodes, respectively. Compared to other two sample, the higher charge carrier density of Co/La:$BiVO_4$ might own to the synergistic effect of doping and oxygen defects. Moreover, the PL spectrum is also an important method to evaluate the photogenerated carrier dynamics of a photocatalyst or a photoelectrode. Thus, the TRPL spectra of pristine $BiVO_4$ and Co/La:$BiVO_4$ are shown in Fig. 5(b). The fitting results (inset in Fig. 5(b)) of a double exponential decay model exhibits that the Co/La:$BiVO_4$ sample owns a shorter average lifetime (1.084 ns) than the pristine $BiVO_4$ one (1.548 ns). This might be ascribed to the fact that the existence of deep levels in the co-doped sample accelerates the recombination of photogenerated carriers. It should be emphasized, however, that the TRPL test was performed on individual samples that were not immersed into the electrolyte for the PEC measurement. As a result, the reduction in TRPL lifetime has nothing to do with the carrier separation that occurs at the electrode/electrolyte interface. In other words, Although the carrier lifetime is shortened by co-doping, the carrier separation efficiency is not significantly affected.

To confirm the photocurrent generated is truly used for OER, H_2 and O_2 produced at the photoanode in 5 h are detected by a gas chromatography as shown in Fig. 5(c). For the Co/La:$BiVO_4$ sample, the H_2 production rate reaches 57.6 μmol cm^{-2} h^{-1}, which is quite close to the result calculated from the photocurrent. The O_2 production rate is 25.8 μmol cm^{-2} h^{-1}, which is slightly lower than the

theoretical value obtained from the calculation. Such a deviation may be due to the O_2 bubbles attached to the surface of the porous $BiVO_4$ electrode. The test results demonstrated that most of the electron-hole pairs participated in the PEC water splitting reaction without recombination. Additionally, the long-term stability is investigated in Fig. 5(d). The photocurrent of Co/La:$BiVO_4$ photoanode remains nearly 93.1% of the initial value after 16 h, while the photocurrent of pristine $BiVO_4$ attenuates to 52.6% just after 12 h. The improvement in the PEC stability should be related to the enhanced photogenerated carrier separation, resulting in fewer holes remaining at the $BiVO_4$ surface. Holes accelerate the transition of V^{5+} to V^{6+}, which is an important cause for the photocorrosion of $BiVO_4$ [22,26]. Moreover, XRD and XPS measurements are carried out on the Co/La:$BiVO_4$ photoanode after a long-term PEC measurement in order to evaluate the stability of the obtained photoanodes, as shown in Fig. S17. The results show that there is almost no change in XRD and XPS spectra even after a long time of PEC reaction, suggesting that the crystal structure of the material isn't damaged during the PEC stability.

4. Summary

In this work, a novel route is developed to *in-situ* dope the "worm-like" $BiVO_4$ electrodes with Co and La. The best performance is shown by the 0.7Co/0.3La:$BiVO_4$ sample, which displays a nearly threefold higher photocurrent (~ 3.65 mA cm^{-2}) than that of $BiVO_4$ (just 1.25 mA cm^{-2}) under the simulated sunlight irradiation. In addition, this photoanode exhibits an excellent stability (retaining 93.1% of the PEC cell performance after 16 h) and low onset potential of 0.1 V_{RHE}. The DFT theoretical calculation and characterization shows that the Co/La:$BiVO_4$ photoanode has the smaller direct bandgap, deep levels and oxygen vacancies, resulting in the higher visible light absorption and more efficient carrier separation at solid/liquid interfaces than other samples. The in-depth analyses reveal that the Co dopant atoms cause the bandgap of $BiVO_4$ to decrease, and the La dopant atoms leads to the bandgap to switch from indirect to direct. The dual-element doping is also benefit for introducing deep levels into the $BiVO_4$ bandgap. Besides, the formed oxygen defect is an innate cocatalyst, contributing to the improved carrier separation and suppression of photocorrosion. This work will contribute to the understanding of the co-doping mechanism as well as to the development of a highly efficient photoanode for unbiased solar water splitting.

CRediT authorship contribution statement

Huimin Geng: Preparation of materials, Methodology, Software. **Sheng Huang**: Data curation, Writing – original draft preparation. **Dan Kong:** Writing – reviewing and editing, valuable suggestions. **Eugene Chubenko**: Visualization, Investigation. **Xiuquan Gu**: Supervision. **Pengzhan Ying**: Software, Theoretical calculation, Validation. **Vitaly Bondarenko**: Writing – reviewing and editing. **Yanwei Sui**: Writing – reviewing and editing. **Yulong Zhao**: Writing – reviewing and editing.

Data availability

Data will be made available on request.

Declaration of Competing Interest

The authors declare that they have no known competing financial interests or personal relationships that could have appeared to influence the work reported in this paper.

Acknowledgement

The authors acknowledge the financial support obtained from Fundamental Research Funds for the Central Universities (2019ZDPY04), Graduate Innovation Program of Jiangsu Province (2021WLJCRCZL165) and Major Research Project of Philosophy and Social Sciences in Colleges and Universities in Jiangsu Province (2020SJZDA122).

Appendix A. Supporting information

Supplementary data associated with this article can be found in the online version at doi:10.1016/j.jallcom.2022.166667.

References

[1] R. Tang, S. Zhou, Z. Zhang, R. Zheng, J. Huang, Engineering nanostructure-interface of photoanode materials toward photoelectrochemical water oxidation, Adv. Mater. 33 (2021) 2005389..
[2] L. Ran, S. Qiu, P. Zhai, Z. Li, J. Gao, X. Zhang, B. Zhang, C. Wang, L. Sun, J. Hou, Conformal macroporous inverse opal oxynitride-based photoanode for robust photoelectrochemical water splitting, J. Am. Chem. Soc. 143 (2021) 7402–7413.
[3] Z.-Q. Wei, S. Hou, S.-C. Zhu, Y. Xiao, G. Wu, F.-X. Xiao, Polymer-mediated electron tunneling towards solar water oxidation, Adv. Funct. Mater. 32 (2022) 2106338.
[4] Z.-Q. Wei, X.-C. Dai, S. Hou, Y.-B. Li, M.-H. Huang, T. Li, S. Xu, F.-X. Xiao, Branched polymer-incorporated multi-layered heterostructured photoanode: precisely tuning directional charge transfer toward solar water oxidation, J. Mater. Chem. A 8 (2020) 177–189.
[5] S. Hou, X.-C. Dai, Y.-B. Li, M.-H. Huang, T. Li, Z.-Q. Wei, Y. He, G. Xiao, F.-X. Xiao, Charge transfer modulation in layer-by-layer-assembled multilayered photoanodes for solar water oxidation, J. Mater. Chem. A 7 (2019) 22487–22499.
[6] M.G. Walter, E.L. Warren, J.R. McKone, S.W. Boettcher, Q. Mi, E.A. Santori, N.S. Lewis, Solar water splitting cells, Chem. Rev. 110 (2010) 6446–6473.
[7] M. Fang, Q.A. Cai, Q. Qin, W. Hong, W. Liu, Mo-doping induced crystal orientation reconstruction and oxygen vacancy on $BiVO_4$ homojunction for enhanced solar-driven water splitting, Chem. Eng. J. 421 (2021) 127796.
[8] J. Feng, J. Bian, L. Bai, S. Xi, Y. Wang, C. Chen, L. Jing, Efficient wide-spectrum photocatalytic overall water splitting over ultrathin molecular nickel phthalocyanine/$BiVO_4$ Z-scheme heterojunctions without noble metals, Appl. Catal. B 295 (2021) 120260.
[9] Z. Zeng, T. Li, Y.-B. Li, X.-C. Dai, M.-H. Huang, Y. He, G. Xiao, F.-X. Xiao, Plasmon-induced photoelectrochemical water oxidation enabled by in situ layer-by-layer construction of cascade charge transfer channel in multilayered photoanode, J. Mater. Chem. A 6 (2018) 24686–24692.
[10] M. Noor, F. Sharmin, M.A.A. Mamun, S. Hasan, M.A. Hakim, M.A. Basith, Effect of Gd and Y co-doping in $BiVO_4$ photocatalyst for enhanced degradation of methylene blue dye, J. Alloy. Compd. 895 (2022) 162639.
[11] C. Liu, H. Luo, Y. Xu, Z. Zhang, Q. Liang, W. Wang, Z. Chen, Synergistic cocatalytic effect of ultra-thin metal-organic framework and Mo-dopant for efficient photoelectrochemical water oxidation on $BiVO_4$ photoanode, Chem. Eng. J. 384 (2020) 123333.
[12] J. Li, H. Yuan, J. Li, W. Zhang, Y. Liu, N. Liu, H. Cao, Z. Jiao, The significant role of the chemically bonded interfaces in $BiVO_4$/ZnO heterostructures for photoelectrochemical water splitting, Appl. Catal. B 285 (2021) 119833.
[13] S. Wang, P. Chen, J.-H. Yun, Y. Hu, L. Wang, An electrochemically treated $BiVO_4$ photoanode for efficient photoelectrochemical water splitting, Angew. Chem. Int. Ed. 56 (2017) 8500–8504.
[14] Y. Li, Q. Mei, Z. Liu, X. Hu, Z. Zhou, J. Huang, B. Bai, H. Liu, F. Ding, Q. Wang, Fluorine-doped iron oxyhydroxide cocatalyst: promotion on the WO_3 photoanode conducted photoelectrochemical water splitting, Appl. Catal. B 304 (2022) 120995.
[15] P.M. Rao, L. Cai, C. Liu, I.S. Cho, C.H. Lee, J.M. Weisse, P. Yang, X. Zheng, Simultaneously efficient light absorption and charge separation in WO_3/$BiVO_4$ core/shell nanowire photoanode for photoelectrochemical water oxidation, Nano Lett. 14 (2014) 1099–1105.
[16] Y. Li, Q. Wang, X. Hu, Y. Meng, H. She, L. Wang, J. Huang, G. Zhu, Constructing NiFe-metal-organic frameworks from NiFe-layered double hydroxide as a highly efficient cocatalyst for $BiVO_4$ photoanode PEC water splitting, Chem. Eng. J. 433 (2022) 133592.
[17] X. Li, M. Kan, T. Wang, Z. Qin, T. Zhang, X. Qian, Y. Kuwahara, K. Mori, H. Yamashita, Y. Zhao, The ClO-generation and chlorate suppression in photoelectrochemical reactive chlorine species systems on $BiVO_4$ photoanodes, Appl. Catal. B 296 (2021) 120387.
[18] J. Jian, Y. Xu, X. Yang, W. Liu, M. Fu, H. Yu, F. Xu, F. Feng, L. Jia, D. Friedrich, R. van de Krol, H. Wang, Embedding laser generated nanocrystals in $BiVO_4$ photoanode for efficient photoelectrochemical water splitting, Nat. Commun. 10 (2019) 2609.
[19] J.-M. Wu, Y. Chen, L. Pan, P. Wang, Y. Cui, D. Kong, L. Wang, X. Zhang, J.-J. Zou, Multi-layer monoclinic $BiVO_4$ with oxygen vacancies and V^{4+} species for highly efficient visible-light photoelectrochemical applications, Appl. Catal. B 221 (2018) 187–195.

[20] X. Hu, Y. Li, X. Wei, L. Wang, H. She, J. Huang, Q. Wang, Preparation of double-layered Co-Ci/NiFeOOH co-catalyst for highly meliorated PEC performance in water splitting, Adv, Powder Mater. 1 (2022) 100024.
[21] B. Zhang, X. Huang, Y. Zhang, G. Lu, L. Chou, Y. Bi, Unveiling the activity and stability origin of $BiVO_4$ photoanodes with FeNi oxyhydroxides for oxygen evolution, Angew. Chem. Int. Ed. 59 (2020) 18990–18995.
[22] D.K. Lee, K.-S. Choi, Enhancing long-term photostability of $BiVO_4$ photoanodes for solar water splitting by tuning electrolyte composition, Nat. Energy 3 (2018) 53–60.
[23] K. Tian, L. Wu, T. Han, L. Gao, P. Wang, H. Chai, J. Jin, Dual modification of $BiVO_4$ photoanode by rare earth element neodymium doping and further $NiFe_2O_4$ co-catalyst deposition for efficient photoelectrochemical water oxidation, J. Alloy. Compd. 923 (2022) 166352.
[24] S. Bai, K. Tian, J.C. Meng, Y. Zhao, J. Sun, K. Zhang, Y. Feng, R. Luo, D. Li, A. Chen, Reduced graphene oxide decorated $SnO_2/BiVO_4$ photoanode for photoelectrochemical water splitting, J. Alloy. Compd. 855 (2021) 156780.
[25] T.W. Kim, K.-S. Choi, Nanoporous $BiVO_4$ photoanodes with dual-layer oxygen evolution catalysts for solar water splitting, Science 343 (2014) 990–994.
[26] S. Wang, T. He, J.-H. Yun, Y. Hu, M. Xiao, A. Du, L. Wang, New iron-cobalt oxide catalysts promoting $BiVO_4$ films for photoelectrochemical water splitting, Adv. Funct. Mater. 28 (2018) 1802685.
[27] B. He, S. Jia, M. Zhao, Y. Wang, T. Chen, S. Zhao, Z. Li, Z. Lin, Y. Zhao, X. Liu, General and robust photothermal-heating-enabled high-efficiency photoelectrochemical water splitting, Adv. Mater. 33 (2021) 2004406.
[28] H. Geng, P. Ying, Y. Zhao, X. Gu, Cactus shaped FeOOH/Au/$BiVO_4$ photoanodes for efficient photoelectrochemical water splitting, Int, J. Hydrog. Energy 46 (2021) 35280–35289.
[29] L. Yang, Y. Xiong, W. Guo, J. Guo, D. Gao, Y. Zhang, P. Xiao, Mo^{6+} doped $BiVO_4$ with improved charge separation and oxidation kinetics for photoelectrochemical water splitting, Electrochim. Acta 256 (2017) 268–277.
[30] F.F. Abdi, L. Han, A.H.M. Smets, M. Zeman, B. Dam, R. van de Krol, Efficient solar water splitting by enhanced charge separation in a bismuth vanadate-silicon tandem photoelectrode, Nat. Commun. 4 (2013) 2195.
[31] S. Liu, R.-T. Gao, R. Zhang, Z. Wang, X. Liu, T. Nakajima, X. Zhang, Y. Su, L. Wang, Tungsten induced defects control on $BiVO_4$ photoanodes for enhanced solar water splitting performance and photocorrosion resistance, Appl. Catal. B 298 (2021) 120610.
[32] M. Tayebi, B.-K. Lee, The effects of W/Mo-co-doped $BiVO_4$ photoanodes for improving photoelectrochemical water splitting performance, Catal. Today 361 (2021) 183–190.
[33] U. Prasad, J. Prakash, S.K. Gupta, J. Zuniga, Y. Mao, B. Azeredo, A.N.M. Kannan, Enhanced photoelectrochemical water splitting with Er- and W-codoped bismuth vanadate with WO_3 heterojunction-based two-dimensional photoelectrode, ACS Appl. Mater. Interfaces 11 (2019) 19029–19039.
[34] W. Jia, Z. Cao, L. Wang, J. Fu, X. Chi, W. Gao, L.-W. Wang, The analysis of a plane wave pseudopotential density functional theory code on a GPU machine, Comput. Phys. Commun. 184 (2013) 9–18.
[35] W. Jia, J. Fu, Z. Cao, L. Wang, X. Chi, W. Gao, L.-W. Wang, Fast plane wave density functional theory molecular dynamics calculations on multi-GPU machines, J. Comput. Phys. 251 (2013) 102–111.
[36] J.P. Perdew, K. Burke, M. Ernzerhof, Generalized gradient approximation made simple, Phys. Rev. Lett. 77 (1996) 3865–3868.
[37] D.R. Hamann, Optimized norm-conserving vanderbilt pseudopotentials, Phys. Rev. B 88 (2013) 085117.
[38] N.T.K. Huyen, T.-D. Pham, N.T.D. Cam, P.V. Quan, N.V. Noi, N.T. Hanh, M.H.T. Tung, V.-D. Dao, Fabrication of titanium doped $BiVO_4$ as a novel visible light driven photocatalyst for degradation of residual tetracycline pollutant, Ceram. Int. 47 (2021) 34253–34259.
[39] K. Kim, J.H. Moon, Three-dimensional bicontinuous $BiVO_4$/ZnO photoanodes for high solar water-splitting performance at low bias potential, ACS Appl. Mater. Interfaces 10 (2018) 34238–34244.
[40] H.S. Park, H.C. Lee, K.C. Leonard, G. Liu, A.J. Bard, Unbiased photoelectrochemical water splitting in Z-scheme device using W/Mo-doped $BiVO_4$ and ZnxCd1-xSe, ChemPhysChem 14 (2013) 2277–2287.
[41] X. Long, L. Gao, F. Li, Y. Hu, S. Wei, C. Wang, T. Wang, J. Jin, J. Ma, Bamboo shoots shaped $FeVO_4$ passivated ZnO nanorods photoanode for improved charge separation/transfer process towards efficient solar water splitting, Appl. Catal. B 257 (2019) 117813.